IET Generation, Transmission & Distribution

Research Article

IET Journals
The Institution of Engineering and Technology

Multi-objective model predictive control of doubly-fed induction generators for wind energy conversion

ISSN 1751-8687
Received on 27th March 2018
Revised 17th July 2018
Accepted on 19th October 2018
E-First on 27th November 2018
doi: 10.1049/iet-gtd.2018.5172
www.ietdl.org

Jiefeng Hu[1], Yong Li[1] ✉, Jianguo Zhu[2]

[1]*Department of Electrical Engineering, The Hong Kong Polytechnic University, Hong Kong, People's Republic of China*
[2]*School of Electrical and Information Engineering, University of Sydney, New South Wales, Australia*
✉ *E-mail: leeo1864@163.com*

Abstract: As large-scale integration of wind systems into the power grid is on the rise, advanced control techniques for wind power generators are highly desired. This paper proposes a simple but effective control technique for doubly fed induction generators (DFIGs) based on the multi-objective model predictive control (MOMPC) scheme. The future behaviors of the DFIGs are predicted by using the system model and the possible converter switching states. The most appropriate vector is then determined by a cost function. By properly modifying the cost function with active and reactive powers as the control objectives, fast grid synchronisation, smooth grid connection, flexible power regulation and maximum power point tracking (MPPT) can be achieved, respectively. In order to reduce the switching frequency for switching loss reduction, a nonlinear constraint is integrated into the cost function. The controller is simple without using any Proportion Integration (PI) regulators, current loops, and switching tables. A numerical simulation of a 2MW system based on MATLAB/Simulink is built to verify the effectiveness of the proposed method. The results show that the proposed method can achieve quicker transient response, better steady-state performance, and lower switching frequency compared to the conventional switching table based direct power control (DPC).

1 Introduction

Wind energy, as a promising renewable energy resource, has attracted much attention. The Global Wind Energy Council (GWEC) Moderate Scenario foresees that the global wind installed capacity reaches 797 GW by 2020, 1676 GW by 2030, and 3984 GW by 2050 [1]. In the global wind market, the doubly-fed induction generator (DFIG) has been widely used due to its merits including maximum power harvest with varying wind speed, decoupled regulation of active and reactive powers, and relatively low overall system cost because of the use of a power electronic converter rated below the system full capacity [2].

As the penetration of renewable energy resources is on the rise, much attention has been paid to system reliability and power quality [3]. In a DFIG-based wind turbine system, the induced stator voltage of the generator should match the grid voltage as close as possible during the grid synchronisation. After the grid connection, the auxiliary grid support capacity of wind energy system should be exploited for the grid stability with high wind power integration [4–6].

Over the last decades, various control methods for DFIGs have been proposed. The most popular one is the field oriented control, also known as the vector control (VC). It regulates the torque (corresponding to the active power) and rotor flux (corresponding to the reactive power) by individually controlling the d- and q-axis components of the rotor current in the synchronous rotary frame [7–10]. However, complex coordinate transformation and modulators such as space vector modulation (SVM) are required. Besides, a large amount of tuning work is needed to obtain satisfactory system stability.

To eliminate the complicated control structure in VC, direct control approaches like the direct torque control (DTC) [11–13] and direct power control (DPC) [14–16] were proposed. Compared to the VC approach, the DTC and DPC algorithms are simpler in terms of the controller structure and have shown faster dynamic response because of the use of a predefined switching table for voltage vector selection to replace the multiple inner voltage/current loops with proportional–integral controllers. However, they produce large torque and power ripples, resulting in oscillating torque and distorted output currents.

In order to overcome the issues mentioned above, various improved strategies have recently been developed to enhance the performance of DFIG under DPC. They can be generally divided into two categories. The first group focuses on the optimisation of modulation methods by applying two or three voltage vectors in every control period [17–19]. The effects of converter voltage vectors on the control variable are first investigated. After that, the durations of the vector sequences are calculated appropriately by various principles, such as equalising the control variable to the reference at the end of the control period, making the mean value of the control variable equal to the reference at the end of the control period, and forcing the root-mean-square value of the control variable to be minimal over one control period. However, the vector sequences are still chosen from a predefined switching table. This means that the vector applied is not necessarily the most effective one to control the system. Zarei *et al.* [20] presented an improved DPC by applying four voltage vectors in every period with the consideration of negative sequence voltage. Even the power ripple is restrained, the calculation of durations of vector sequences is very complicated and subject to the machine parameter variations.

The second group of research focuses on the optimisation of vector selection. In other words, the vector sequences are determined according to the specified criteria rather than a pre-defined switching table. Among these methods, the most popular one is the model predictive control (MPC) [21, 22]. In MPC, the selection criteria of control pattern is defined and the voltage vector that minimises a predefined cost function is chosen for the control. By formulating the cost function properly, various control objectives and different system constraints can be included [23–25]. More recently, various improved MPC methods have been developed to further enhance the DFIG performance by eliminating the offset between the reference and the actual value [24].

All the DFIG control methods mentioned above, however, do not consider the process of grid synchronisation. Fast synchronisation and smooth grid connection are crucial because wind power generators need to be disconnected and reconnected to the grid under different operation conditions [26–28]. Besides, the control approaches mentioned above are only tested at certain rotor speeds. The practical effects of wind turbine on DFIG at various

wind speeds need to be considered in order to demonstrate the feasibility of the control. Another important issue in wind energy systems is the power loss. As the large-scale integration of wind turbine systems into the grid is on the rise, together with the upscaling of the single wind turbine power capacity, power efficiency has become a major concern [29, 30]. To reduce the switching loss and hence, increase the efficiency, low converter switching frequency is desirable, especially in high power applications [31].

To the best of authors' knowledge, there is no existing work considering a detailed comprehensive MPC approach for high-power DFIG-based wind energy systems where grid synchronisation, grid-connected operation and switching frequency reduction are all addressed in one controller. The major contribution of this work is to extend and explore the feasibility of MPC on DFIGs and to advance one step further by proposing a multi-objective MPC (MOMPC) strategy. Fast grid synchronisation, smooth grid connection, flexible power regulation, and maximum power point tracking (MPPT) can all be achieved by using only one cost function format with active and reactive powers as the control objectives. Meanwhile, the average switching frequency of the DFIG converter can be maintained at a low level with the purpose of reducing switching loss.

2 Wind turbine and DFIG modelling

The DFIG-based variable-speed wind energy system under study consists of a wind turbine, DFIG, and a back-to-back power electronic converter. The output mechanical power of the wind turbine, P_{m}, can be determined by [7]

$$P_{\mathrm{m}} = 0.5\rho A C_{\mathrm{p}} v_{\mathrm{w}}^3 \tag{1}$$

where C_{p} is the power coefficient of the turbine, which is a function of the tip-speed ratio (TSR) and the pitch angle (β), ρ is the mass density of air (kg/m^3), A is the turbine swept area (m^2), and v_{w} is the wind speed (m/s). The TSR is defined as

$$\mathrm{TSR} = \frac{R\omega_{\mathrm{m}}}{v_{\mathrm{w}}} \tag{2}$$

where R is the radius of the turbine and ω_{m} is the turbine shaft speed in radians per second. The wind turbine can harvest maximum wind energy when it operates at the optimal power coefficient. Therefore, it is necessary to keep the rotor speed at an optimum value of the TSR. In other words, the rotor speed is contingent on how fast the winds blow.

For the DFIG-based wind system, the wind power is injected into the grid via the stator and the rotor is fed by a back-to-back power electronic converter. A constant DC-bus voltage is obtained by converting the grid AC voltage through the grid-side converter, based on which the rotor-side converter is used to regulate the rotor current. The mathematical equations for a DFIG can be expressed in either the stationary stator-oriented reference frame or the rotary rotor-oriented synchronous frame using complex vectors. Here they are quoted as follows in the rotary synchronous frame.

The voltage equations:

$$\boldsymbol{V}_{\mathrm{s}} = R_{\mathrm{s}}\boldsymbol{I}_{\mathrm{s}} + \frac{\mathrm{d}\boldsymbol{\psi}_{\mathrm{s}}}{\mathrm{d}t} + j\omega_{\mathrm{r}}\boldsymbol{\psi}_{\mathrm{s}} \tag{3}$$

$$\boldsymbol{V}_{\mathrm{r}} = R_{\mathrm{r}}\boldsymbol{I}_{\mathrm{r}} + \frac{\mathrm{d}\boldsymbol{\psi}_{\mathrm{r}}}{\mathrm{d}t} \tag{4}$$

The flux equations:

$$\boldsymbol{\psi}_{\mathrm{s}} = L_{\mathrm{s}}\boldsymbol{I}_{\mathrm{s}} + L_{\mathrm{m}}\boldsymbol{I}_{\mathrm{r}} \tag{5}$$

$$\boldsymbol{\psi}_{\mathrm{r}} = L_{\mathrm{m}}\boldsymbol{I}_{\mathrm{s}} + L_{\mathrm{r}}\boldsymbol{I}_{\mathrm{r}} \tag{6}$$

The electromagnetic torque equation:

$$T_{\mathrm{e}} = \frac{3}{2}p\mathrm{Im}\{\boldsymbol{\psi}_{\mathrm{s}}^{*}\mathbf{I}_{\mathrm{s}}\} \tag{7}$$

The stator output powers equations:

$$P = \frac{3}{2}\omega_1\lambda L_{\mathrm{m}}\mathrm{Im}\{\boldsymbol{\psi}_{\mathrm{r}}^{*}\boldsymbol{\psi}_{\mathrm{s}}\} \tag{8}$$

$$Q = \frac{3}{2}\omega_1\lambda[L_{\mathrm{r}}|\boldsymbol{\psi}_{\mathrm{s}}|^2 - L_{\mathrm{m}}\mathrm{Re}\{\boldsymbol{\psi}_{\mathrm{r}}^{*}\boldsymbol{\psi}_{\mathrm{s}}\}] \tag{9}$$

where $\lambda = 1/(L_{\mathrm{s}}L_{\mathrm{r}} - L_{\mathrm{m}}^2)$, ω_{r} and ω_1 are the rotor angular speed and grid angular frequency, $\boldsymbol{V}_{\mathrm{s}}$ and $\boldsymbol{V}_{\mathrm{r}}$ are the voltage vectors, $\boldsymbol{I}_{\mathrm{s}}$ and $\boldsymbol{I}_{\mathrm{r}}$ are the current vectors, R_{s} and R_{r} are the winding resistances, $\boldsymbol{\psi}_{\mathrm{s}}$ and $\boldsymbol{\psi}_{\mathrm{r}}$ are the flux vectors, L_{s} and L_{r} are the self-inductances, and $L_{\sigma\mathrm{s}}$ and $L_{\sigma\mathrm{r}}$ are the leakage inductances of the stator and rotor, respectively, L_{m} is the magnetisation inductance, p is the number of pole pairs, and * is the complex conjugate operator.

The derivatives (or the changing rate) of the active and reactive powers with respect to time t can be derived from (8) and (9) as

$$\begin{aligned}\frac{\mathrm{d}P}{\mathrm{d}t} = \frac{3}{2}\omega_1\lambda L_{\mathrm{m}}[&\mathrm{Im}\{\boldsymbol{V}_{\mathrm{r}}^{*}\boldsymbol{\psi}_{\mathrm{s}}\} + \omega_{\mathrm{s}}\mathrm{Re}\{\boldsymbol{\psi}_{\mathrm{r}}^{*}\boldsymbol{\psi}_{\mathrm{s}}\} \\ &- \lambda R_{\mathrm{r}}L_{\mathrm{s}}\mathrm{Im}\{\boldsymbol{\psi}_{\mathrm{r}}^{*}\boldsymbol{\psi}_{\mathrm{s}}\}]\end{aligned} \tag{10}$$

and

$$\begin{aligned}\frac{\mathrm{d}Q}{\mathrm{d}t} = -\frac{3}{2}\omega_1\lambda L_{\mathrm{m}}[&\mathrm{Re}\{\boldsymbol{V}_{\mathrm{r}}^{*}\boldsymbol{\psi}_{\mathrm{s}}\} - \omega_{\mathrm{s}}\mathrm{Im}\{\boldsymbol{\psi}_{\mathrm{r}}^{*}\boldsymbol{\psi}_{\mathrm{s}}\} \\ &- \lambda R_{\mathrm{r}}L_{\mathrm{s}}\mathrm{Re}\{\boldsymbol{\psi}_{\mathrm{r}}^{*}\boldsymbol{\psi}_{\mathrm{s}}\} + \lambda R_{\mathrm{r}}L_{\mathrm{m}}|\boldsymbol{\psi}_{\mathrm{s}}|^2]\end{aligned} \tag{11}$$

3 Comparison of DPC and MPC for DFIG

3.1 Principle of conventional switching table based DPC

In a two-level inverter, there are eight possible voltage vectors (six active vectors and two null vectors). According to (10) and (11), the system output active and reactive powers can be regulated by applying proper voltage vectors subject to the rotor flux position. To achieve this, a switching table for voltage vector selection is employed, as shown by the block diagram in Fig. 1*a*, where *Sk* is the number of sector in which the rotor flux is. In fact, the switching table introduced in [15] is equivalent to those in [19]. It should be noted that at the hyper-synchronous speed the rotor flux is rotating in the opposite direction to that at the sub-synchronous speed.

The DPC uses the errors between the estimated actual output active and reactive powers, P and Q, and the references, $P_{\_\mathrm{ref}}$ and $Q_{\_\mathrm{ref}}$, to determine whether to increase or decrease them by using the digitised signals d_P and d_Q from the hysteresis comparators. The voltage vector is then selected from the switching table according to d_Q, d_P and the number of sector in which the rotor flux is located. Finally, the pulse-width modulation (PWM) signal is generated according to the selected voltage vector to control the rotor-side converter.

3.2 Principle of MPC

In the MPC, the system plant can be described by a discrete-time state-space model. The future behaviour of the system is predicted by the input, the present state of the model, and the discrete interval. A cost function is then formulated to evaluate each switching state, and the one forcing the controlled variable as close as possible to the reference will be applied in the next control period.

For the DFIG, substituting (4) into (10) and (11) yields the following approximate form of power derivatives:

$$\frac{\mathrm{d}P}{\mathrm{d}t} = \frac{3}{2}\omega_1\lambda L_{\mathrm{m}}[\mathrm{Im}\{\boldsymbol{V}_{\mathrm{r}}^{*}\boldsymbol{\psi}_{\mathrm{s}}\} + \omega_{\mathrm{s}}\mathrm{Re}\{\boldsymbol{\psi}_{\mathrm{s}}\boldsymbol{\psi}_{\mathrm{r}}^{*}\}] = f_p \tag{12}$$

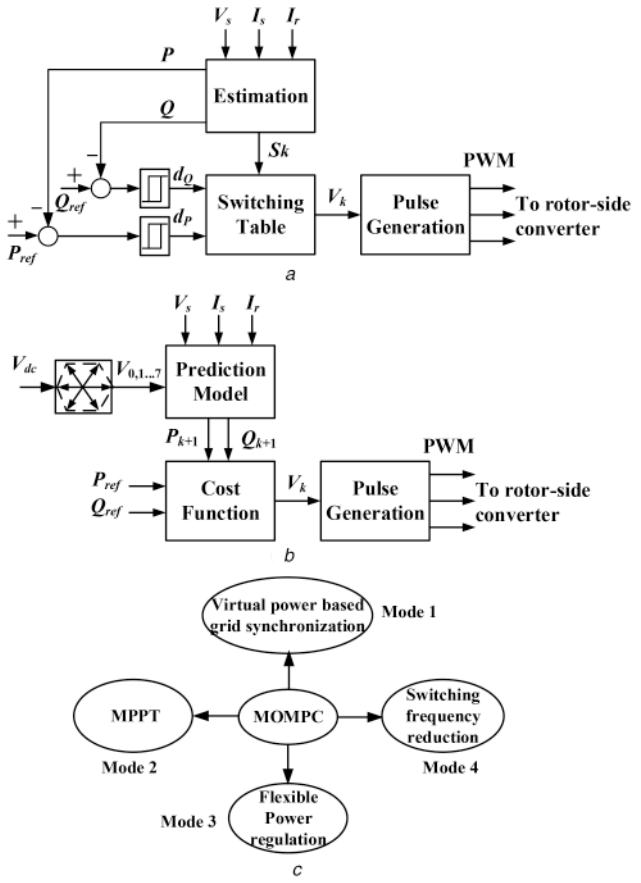

Fig. 1 *Block diagram*
(a) DPC controller for DFIGs, ***(b)*** MPC for DFIGs, ***(c)*** Schematic illustration of MOMPC concept for DFIG-based wind energy system

$$\frac{\mathrm{d}Q}{\mathrm{d}t} = -\frac{3}{2}\omega_1 \lambda L_\mathrm{m}[\mathrm{Re}\{\boldsymbol{V}_\mathrm{r}^*\boldsymbol{\psi}_\mathrm{s}\} - \omega_\mathrm{s}\mathrm{Im}\{\boldsymbol{\psi}_\mathrm{r}^*\boldsymbol{\psi}_\mathrm{s}\}] = f_q \tag{13}$$

It can be seen that the DFIG model uses the active and reactive powers as the state variables and the rotor voltage as the input. Based on this discrete-time model, the active and reactive powers at the next sampling instant can be predicted as

$$P^{k+1} = P^k + f_p T_\mathrm{s} \tag{14}$$

$$Q^{k+1} = Q^k + f_q T_\mathrm{s} \tag{15}$$

where T_s is the sampling period. Fig. 1*b* depicts the principle of the MPC controller for DFIG. The essential of the MPC for DFIG is to evaluate the effects of all the possible inverter voltage vectors on the stator output powers. The voltage vector that can result in the smallest value of a specified cost function will then be selected and applied. The cost function can be defined in various forms. For the power control of DFIG, the cost function can be formulated as

$$\begin{aligned} \min \ \cdot g &= (P_\mathrm{ref} - P^{k+1})^2 + (Q_\mathrm{ref} - Q^{k+1})^2 \\ V_\mathrm{r}^k &\in \{V_0, V_1, \ldots, V_6, V_7\} \end{aligned} \tag{16}$$

where P_ref and Q_ref are the reference values of active and reactive powers. It should be noted that the cost functions take different forms for grid synchronisation, flexible power regulation, and switching frequency reduction. This will be further developed in Section 4.

The MPC is more accurate and effective than the conventional switching-table-based DPC because it uses the complete model of DFIG and converter. In the DPC, at every control instant, the control is determined by looking up the voltage vector from a pre-defined switching table. Consequently, the selected vector is not necessarily the best one to reduce the active and reactive powers ripples. The MPC, on the other hand, selects the voltage vector by optimising a cost function such that the control priority can be weighted flexibly.

4 Proposed MOMPC

The proposed MOMPC concept is explained schematically in Fig. 1*c*. When the wind speed reaches the cut-in threshold, the grid synchronisation should start immediately for fast and smooth grid connection. After grid connection, the generator is usually controlled to output maximum power with the fluctuating wind speed. Besides the basic MPPT operation, the wind generator should be able to generate active and reactive powers flexibly according to the grid status. Also, the converter switching frequency should be minimised as much as possible to increase energy conversion efficiency.

4.1 Virtual power for grid synchronisation (mode 1)

The smooth connection of the DFIG to the power grid requires the fulfilment of three conditions, i.e. the frequency, magnitude, and phase angle of the induced stator terminal voltage must be synchronised to the grid voltage. Before connected to the grid, the stator terminal is open circuited. The dynamic equations of DFIG can be derived from (3)–(6) as

$$\boldsymbol{V}_\mathrm{s} = \frac{\mathrm{d}\boldsymbol{\psi}_\mathrm{s}}{\mathrm{d}t} + j\omega_\mathrm{r}\boldsymbol{\psi}_\mathrm{s} \tag{17}$$

$$\boldsymbol{V}_\mathrm{r} = R_\mathrm{r}\boldsymbol{I}_\mathrm{r} + \frac{\mathrm{d}\boldsymbol{\psi}_\mathrm{r}}{\mathrm{d}t} \tag{18}$$

$$\boldsymbol{\psi}_\mathrm{s} = L_\mathrm{m}\boldsymbol{I}_\mathrm{r} \tag{19}$$

$$\boldsymbol{\psi}_\mathrm{r} = L_\mathrm{r}\boldsymbol{I}_\mathrm{r} \tag{20}$$

The virtual power concept was proposed in [11], but it has seldom been utilised ever since. Here, the virtual power concept is adopted to meet the requirements of grid synchronisation. The virtual grid flux is defined as

$$\boldsymbol{\psi}_\mathrm{g} = \int \boldsymbol{V}_\mathrm{g}\,\mathrm{d}t \tag{21}$$

where $\boldsymbol{V}_\mathrm{g}$ is the grid voltage vector. Similar to the actual output active and reactive powers of DFIG described by (8) and (9), the virtual powers of DFIG can be expressed as

$$P_v = \frac{3}{2}\omega_1 \lambda L_\mathrm{m}\mathrm{Im}\{\boldsymbol{\psi}_\mathrm{r}^*\boldsymbol{\psi}_\mathrm{g}\} \tag{22}$$

$$Q_v = \frac{3}{2}\omega_1 \lambda [L_\mathrm{r}|\boldsymbol{\psi}_\mathrm{g}|^2 - L_\mathrm{m}\mathrm{Re}\{\boldsymbol{\psi}_\mathrm{r}^*\boldsymbol{\psi}_\mathrm{g}\}] \tag{23}$$

The stator flux can be derived from the stator voltage by

$$\boldsymbol{\psi}_\mathrm{s} = \int \boldsymbol{V}_\mathrm{s}\,\mathrm{d}t \tag{24}$$

According to (21) and (24), equality in phase and frequency between $\boldsymbol{V}_\mathrm{s}$ and $\boldsymbol{V}_\mathrm{g}$ is equivalent to the equality in phase and frequency between $\boldsymbol{\psi}_\mathrm{s}$ and $\boldsymbol{\psi}_\mathrm{g}$. Since the stator current is zero before grid connection, which means $P = 0$. Consequently, the angle between the stator flux $\boldsymbol{\psi}_\mathrm{s}$ and rotor flux $\boldsymbol{\psi}_\mathrm{r}$ is zero according to (8). In other words, $\boldsymbol{\psi}_\mathrm{s}$ and $\boldsymbol{\psi}_\mathrm{r}$ are in phase. Thus, controlling $\boldsymbol{\psi}_\mathrm{r}$ to be in-phase with $\boldsymbol{\psi}_\mathrm{g}$ will automatically drive $\boldsymbol{\psi}_\mathrm{s}$ to be in-phase with $\boldsymbol{\psi}_\mathrm{g}$ and hence, $\boldsymbol{V}_\mathrm{s}$ will be in-phase with $\boldsymbol{V}_\mathrm{g}$. Based on this analysis, the first two grid synchronisation conditions can be met by controlling $\boldsymbol{\psi}_\mathrm{r}$ to be in-phase with $\boldsymbol{\psi}_\mathrm{g}$. This can be done by controlling δ (the angle between $\boldsymbol{\psi}_\mathrm{g}$ and $\boldsymbol{\psi}_\mathrm{r}$) to zero, which can be fulfilled by regulating P_v equal to zero as

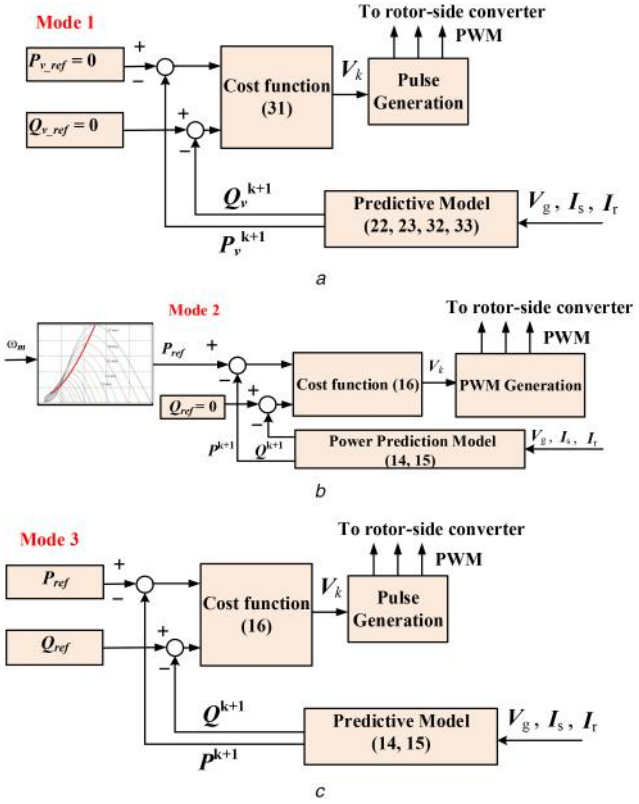

Fig. 2 *Control scheme*

(a) Mode 1 – virtual power based grid synchronisation of the proposed MOMPC strategy, ***(b)*** Mode 2 – MPPT of the proposed MOMPC strategy, ***(c)*** Mode 3 – flexible power regulation of the proposed MOMPC strategy

$$P_v = \frac{3}{2}\omega_1 \lambda L_m \mathrm{Im}\{\boldsymbol{\psi}_r^* \boldsymbol{\psi}_g\} = \frac{3}{2}\omega_1 \lambda L_m |\boldsymbol{\psi}_r||\boldsymbol{\psi}_g| \sin\delta = 0 \tag{25}$$

Next, let us achieve the third grid synchronisation condition, i.e. the equality in magnitude between the stator induced voltage and the grid voltage. From (19) and (20), the relationship between the rotor and grid fluxes can be obtained as

$$\boldsymbol{\psi}_r = \frac{L_r}{L_m}\boldsymbol{\psi}_s \tag{26}$$

Based on (21) and (24), if the DFIG stator voltage must match the grid voltage for grid synchronisation, $\boldsymbol{\psi}_s = \boldsymbol{\psi}_g$ must be obtained. As a result, (26) becomes

$$\boldsymbol{\psi}_r = \frac{L_r}{L_m}\boldsymbol{\psi}_g \tag{27}$$

From (21), the relationship between the grid flux and grid voltage can be rewritten as

$$\boldsymbol{\psi}_g = \frac{\boldsymbol{V}_g}{j\omega_1} \tag{28}$$

Substituting (28) into (27), one obtains the required rotor flux magnitude to achieve the third synchronisation condition as

$$|\boldsymbol{\psi}_r| = \frac{L_r |\boldsymbol{V}_g|}{L_m \omega_1} \tag{29}$$

Substituting (29) into (23), one obtains

$$Q_v = \frac{3}{2}\omega_1 \lambda [L_r |\boldsymbol{\psi}_g|^2 - L_m \mathrm{Re}\{\boldsymbol{\psi}_r^* \boldsymbol{\psi}_g\}] = 0 \tag{30}$$

Therefore, the third synchronisation condition, the equality of voltage magnitude, can be met by controlling Q_v to zero.

To control P_v and Q_v to zero simultaneously, the cost function (16) should be rewritten as

$$\begin{aligned} \min \ \cdot g &= (0 - P_v^{k+1})^2 + (0 - Q_v^{k+1})^2 \\ V_r^k &\in \{V_0, V_1, \ldots, V_6, V_7\} \end{aligned} \tag{31}$$

Fig. 2*a* illustrates the control diagram of grid synchronisation. After the design of the cost function, the prediction model to predict P_v^{k+1} and Q_v^{k+1} is needed. Under the assumption of sinusoidal and balanced grid voltage, $\mathrm{d}\boldsymbol{V}_g/\mathrm{d}t = j\omega_1 \boldsymbol{V}_g$, and thus $\boldsymbol{V}_g^{k+1} = \boldsymbol{V}_g^k + j\omega_1 \boldsymbol{V}_g^k$. Subsequently, the grid flux $\boldsymbol{\psi}_g^{k+1}$ can be predicted as

$$\boldsymbol{\psi}_g^{k+1} = \frac{\boldsymbol{V}_g^{k+1}}{j\omega_1} \tag{32}$$

The rotor flux $\boldsymbol{\psi}_r^{k+1}$ can be predicted from (18) and (20) as

$$\boldsymbol{\psi}_r^{k+1} = L_r\left[I_r^k + \frac{T_s}{L_r}\left(V_r^k - R_r I_r^k\right)\right] \tag{33}$$

Therefore, P_v^{k+1} and Q_v^{k+1} can be predicted by substituting (32) and (33) into (22) and (23), respectively. When the grid synchronisation conditions are met, the stator terminal can be connected to the grid. The generator is then ready to supply power to the power grid.

4.2 MPPT for grid-connected operation (mode 2)

After grid connection, the generator can operate in the MPPT mode, which is the most common case in wind power generation systems. The active power reference is obtained for a given wind speed from the look-up table of the maximum power versus rotor speed characteristic of the wind turbine. This look-up table can be obtained offline from the wind turbine manufactory beforehand. Since the analysis in Section 3.2 is based on the grid-connected operation, (8)–(16) can be used here. Fig. 2*b* shows a block diagram of MPPT under grid-connected operation. From mode 1 to mode 2, the controller can be modified by simply replacing the cost function (31) with (16) and replacing the virtual power references with the actual power references from the MPPT characteristic without changing the control system structure.

4.3 Flexible power regulation for grid-connected operation (mode 3)

In addition to unity power factor operation, wind energy systems can also provide reactive power compensation to the power grid for voltage support and power quality improvement, and thus the system can be operated in the off-MPPT mode when the power generation exceeds the power demanded. Flexible regulation of the active and reactive powers is therefore preferable. Fig. 2*c* illustrates a block diagram of this control. In this operating mode, P_{ref} and Q_{ref} can be set to any values as long as the apparent power is within the rated capacity of the DFIG.

4.4 Switching frequency reduction (mode 4)

For large capacity wind energy systems, the power converter switching loss cannot be ignored. In this paper, in order to minimise the switching loss, the cost function (16) can be modified as

$$\begin{aligned} J = {} & (P_{ref} - P^{k+1})^2 + (Q_{ref} - Q^{k+1})^2 \\ & + \lambda_2 \left(\sum_{i=a,b,c} \left| D_i^{k+1} - D_i^k \right| \right) \end{aligned} \tag{34}$$

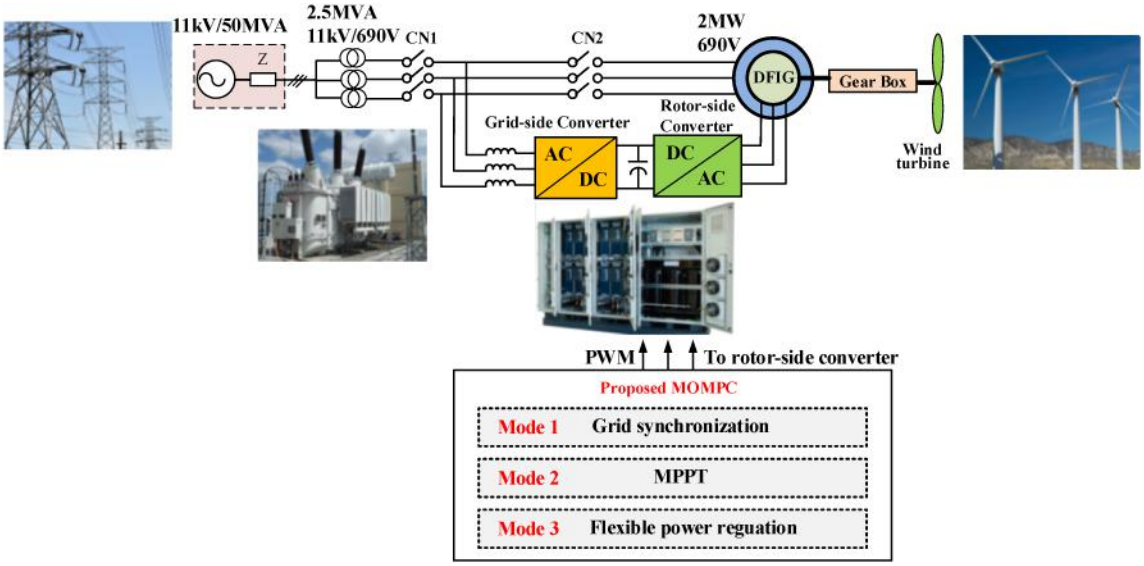

Fig. 3 *Configuration of DFIG-based wind turbine system and the proposed MOMPC*

Table 1 System parameters

DFIG	grid voltage, V_{gN}	11 kV
	rated power, P_N	2 MW
	stator rate voltage, V_N	690 V
	stator resistance, R_s	0.0108 pu
	rotor resistance, R_r	0.0121 pu
	mutual inductance, L_m	3.362 pu
	stator leakage inductance, $L_{\sigma s}$	0.102 pu
	rotor leakage inductance, $L_{\sigma r}$	0.11 pu
	number of pole pairs, p	2
	DC-link nominal voltage, V_{dc}	1200 V
	DC-link capacitance, C_{dc}	16,000 μF
	grid frequency, $f1$	50 Hz
wind turbine	rated power, P_{mN}	2 MW
	air density, ρ	1.225 kg/m^3
	blade radius, R	35.04 m
	base wind speed, V_{wN}	12 m/s
	turbine coefficient, C_p	0.49

where λ_2 is the weighting factor, D_i^k and D_i^{k+1} represent the current and next switching states of the converter leg at phase i ($i = a, b, c$), respectively, $D_i = 0$ indicates that the upper transistor is off and the bottom one is on, and vice versa. By taking the absolute operation of $(D_i^{k+1} - D_i^k)$ on each converter leg, the total switching in every control instant can be computed accurately. As a whole, the first two terms in (34) are aimed to control the active and reactive powers, while the third one contributes to the switching loss reduction by reducing the switching frequency. It is worth mentioning that the weighting factor, λ_2, should be selected carefully through a tradeoff between the power ripple reduction and switching frequency reduction. Since the scope of this paper does not include the weighting factor optimisation, the value of λ_2 will be simply provided in the test.

5 Simulation results

5.1 Complete wind system model

The performance of the proposed control strategy was demonstrated by numerical simulation of a 2 MW DFIG in the MATLAB/Simulink environment, as shown in Fig. 3. The parameters of the DFIG and the wind turbine are listed in Table 1. For the sake of simplicity, the pitch angle of the wind turbine is set to 0°. The gearbox ratio is set to 1:1. The DFIG stator is connected directly to the grid while the rotor is fed by two three-phase two-level bidirectional AC–DC converters connected back-to-back. The 11 kV distribution network model is adapted here as the power grid. It is stepped down to 690 V by using a three-phase transformer to match the voltage level of the wind power generator.

5.2 Overall control strategy

At the beginning of the system operation, CN1 is turned ON and the constant DC-link voltage is first established by the grid-side converter. After the DC-link voltage stabilises at a desired value, the proposed MOMPC algorithm can start to operate by activating the rotor-side converter. When the wind speed reaches the minimum cut-in speed, the control system starts to operate. The virtual active and reactive powers are first estimated and delivered to the cost function (31). When the induced stator voltage can track the grid voltage closely, CN2 is switched ON for grid connection. After the grid connection, the control system switches to the generation mode by simply replacing the virtual powers control loop with the actual powers control loop, and changing the cost function from (31) to (16) for MPPT or flexible power regulation. If required, the cost function (34) can be further adopted to focus on the switching frequency reduction.

Regarding the converter gate driving pulse generation, no PWM modulators such as sinusoidal PWM and SVM are required. Take $\boldsymbol{V}_2(110)$ for example. Once it is selected, it can be generated by just simply turning on the upper switches and turning off the bottom switches of legs A and B, and turning off the upper switch and turning on the bottom switch of leg C of the inverter.

5.3 Grid synchronisation

The virtual power concept has been adopted for the DFIG grid synchronisation. To evaluate the effectiveness of the proposed MOMPC for grid synchronisation, a comprehensive comparison between DPC and MOMPC was carried out. The DFIG started the grid synchronisation at 0.05 s. Fig. 4 shows the stator induced voltage and the rotor current. As shown, the stator voltage by using MOMPC can track the grid voltage more tightly and presents much less distortion and harmonics. In addition, the induced stator voltage of MOMPC can reach the reference in only about 5 ms, while the stator voltage of DPC reaches the reference in ∼10 ms after the grid synchronisation algorithm starts at 0.05 s. These demonstrate the smoother and faster grid synchronisation of MOMPC.

As a further comparison of the stator voltage during grid synchronisation, Fig. 5 presents a harmonic spectrum analysis of the stator voltages. It can be seen that the harmonics concentrate

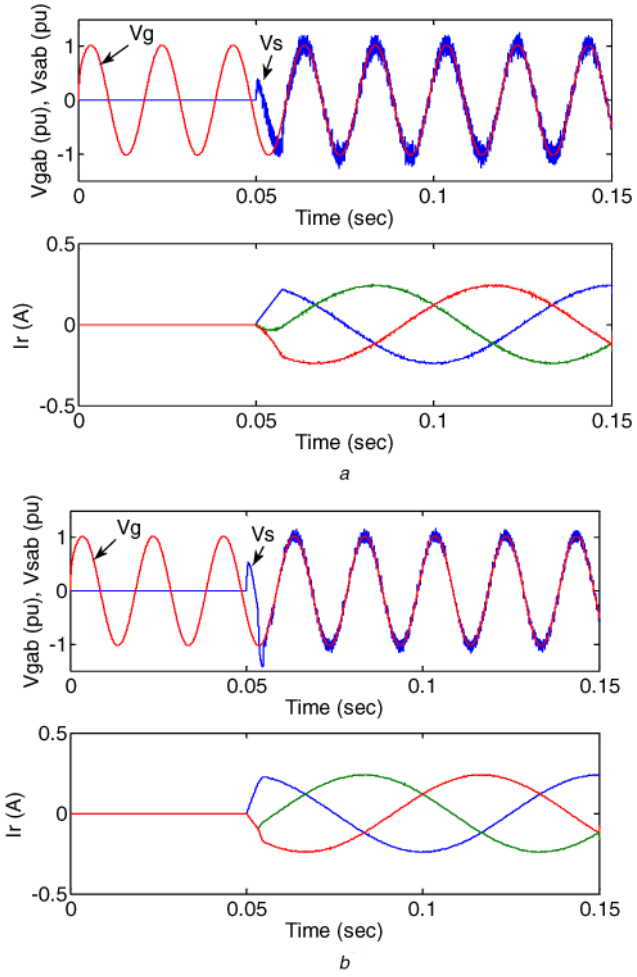

Fig. 4 *Responses of stator induced voltages and rotor currents when system starts the grid synchronisation*
(a) Under DPC, ***(b)*** Under MOMPC

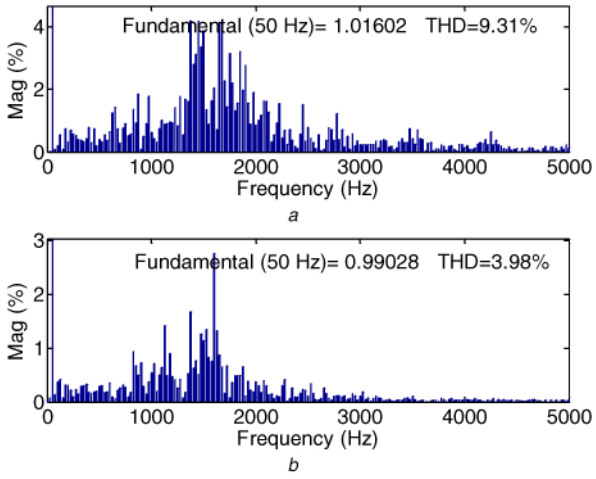

Fig. 5 *Stator voltage spectrums*
(a) Under DPC, ***(b)*** Under MOMPC

around the switching frequencies for both cases. However, compared to DPC, the harmonic spectrum of MOMPC is much clearer, and the stator voltage total harmonic distortion (THD) of MOMPC is only 3.98%, much lower than 9.31% of DPC.

5.4 Grid connection

Once the stator voltage matches the grid voltage in terms of frequency, magnitude, and phase angle, the DFIG can proceed to achieve grid connection. It is important to emphasise that during the grid connection, the virtual powers control loop is still

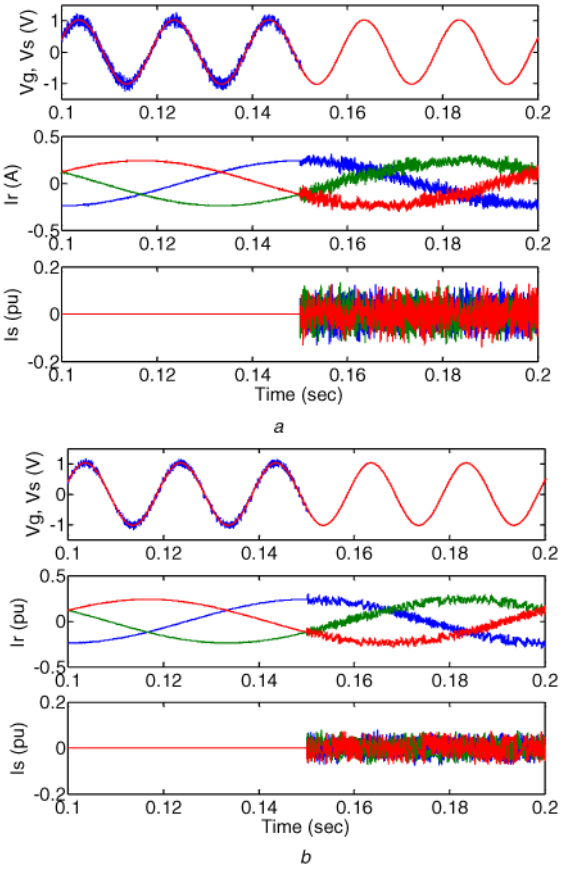

Fig. 6 *Responses of grid connection*
(a) Under DPC, ***(b)*** Under MOMPC

activated, and the virtual active and reactive powers are still controlled to zero. Fig. 6 presents the dynamic response of grid connection at 0.15 s. It is found that no overshoot is observed in the currents in both control methods. Therefore, both control techniques permit a safe grid connection. The main advantage of MOMPC over DPC concentrates on the power quality in the rotor and stator currents after grid connection.

5.5 MPPT operation

The DFIG input is set as torque, which means that the rotor speed is the result of both generator electromagnetic torque and the mechanical torque driven by the wind turbine.

The wind speed ramps from 8 m/s at 1 s to 12 m/s at 3 s. To achieve the MPPT, the active power reference is obtained from the predefined maximum power tracking curve of the wind turbine. The reactive power reference is kept at −0.3 MVar, which means that the DFIG also inject reactive power to the grid during power generation. Fig. 7 shows the complete system performance in this scenario for a longer duration. From top to bottom, the waveforms presented in Fig. 7 are the wind speed, DFIG rotor speed, stator active power output, stator reactive power output, stator current, and rotor current, respectively. It can be seen that when the wind speed increases, the DFIG rotor speed increases gradually from 1 s and reaches the steady-state value at around 9 s because of the inertia. Consequently, the DFIG increases its active power output in the MPPT manner accordingly and generates the rated power of 2 MW eventually. As can be seen, the stator and rotor currents increase smoothly without overshoot. Notice that the rotor current shows DC features at around 3.6 s because the generator reaches the synchronous speed at that instant.

5.6 Flexible power regulation

During this test, the DFIG rotor speed is 1200 rpm and the switching frequency reduction scheme has been used, unless explicitly indicated. First, the steady-state performance will be evaluated. The stator active power reference was set to rated power

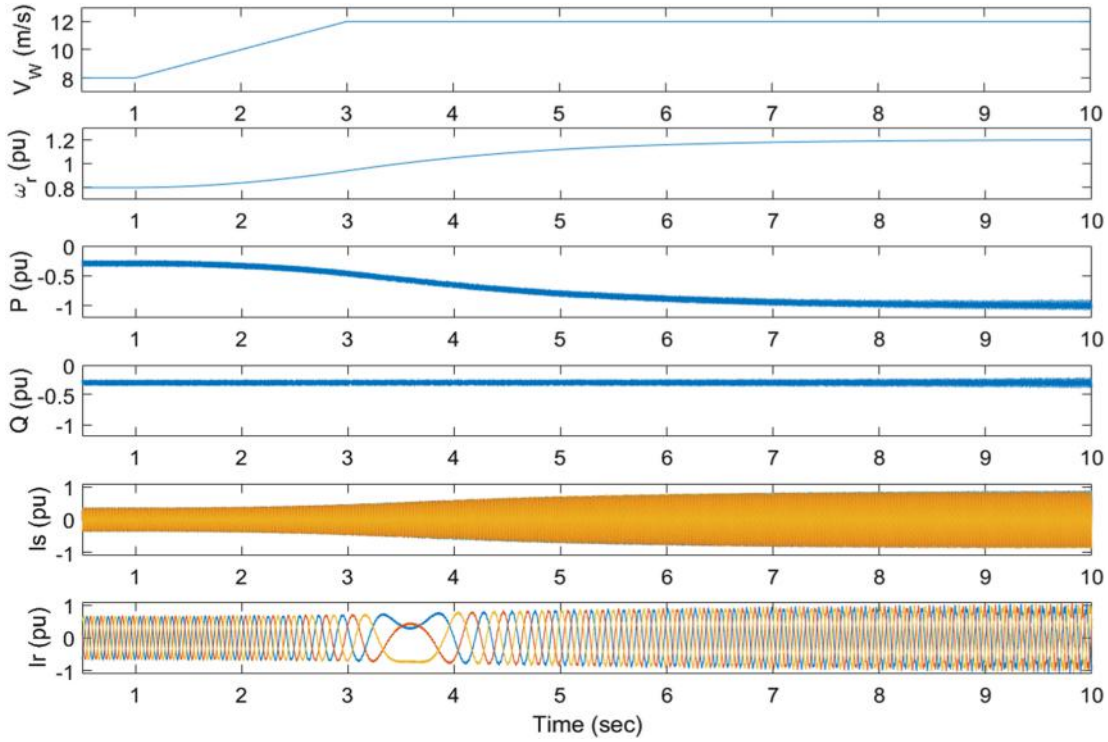

Fig. 7 *Performance of DFIG driven by wind turbine under various wind speed*

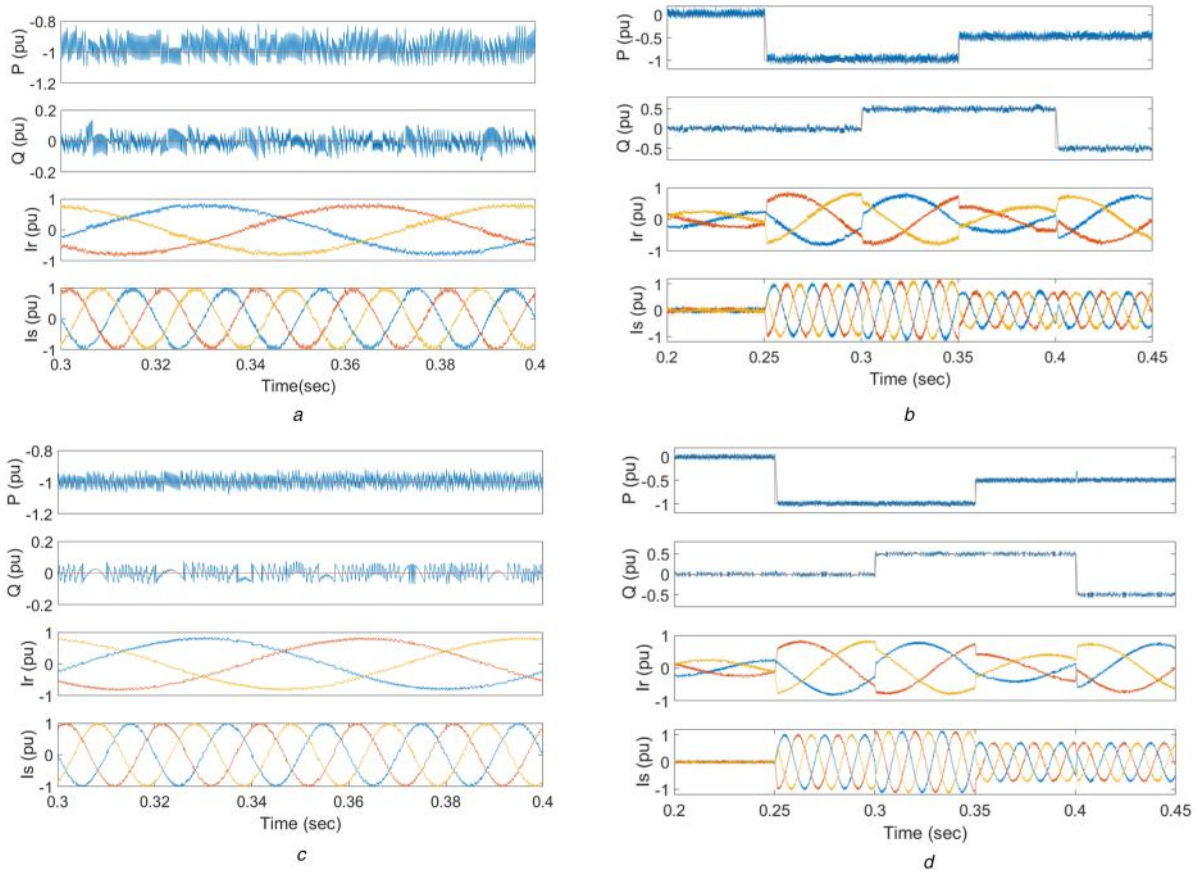

Fig. 8 *Steady-state and dynamic performance of different methods*

(a) Steady-state performance of DPC, ***(b)*** Steady-state performance of MOMPC, ***(c)*** Dynamic performance of DPC, ***(d)*** Dynamic performance of MOMPC

at −2 MW (negative values indicate the injection of power into the grid) and the reactive power reference was set to 0 Mvar. Figs. 8*a* and *b* show the steady-state performance for both methods. As MOMPC evaluates all switching states and selects the optimal voltage vector in every control period according to the cost function, it is able to control the active and reactive powers more effectively with smaller power ripples. As a result, both the stator and rotor currents using MOMPC are more sinusoidal.

The dynamic responses are simulated under a severe active power variation demand to test the quick and safe characteristics of control methods. The active power reference dropped down from 0 to −1 pu at 0.25 s and then stepped up to −0.5 pu at 0.35 s. On the other hand, the reactive power reference stepped up from 0 to 0.5

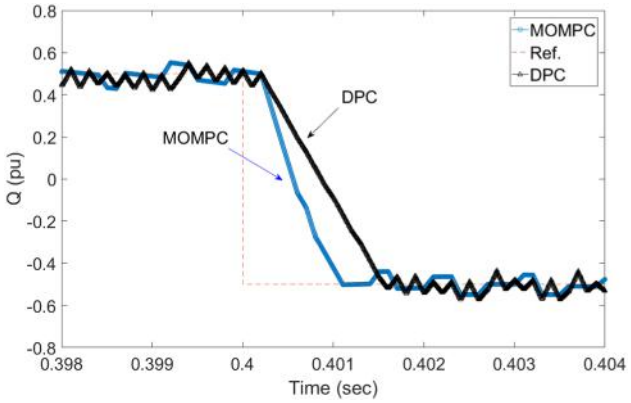

Fig. 9 *Zoom-in responses of DPC and MOMPC with stepped change of reactive powers*

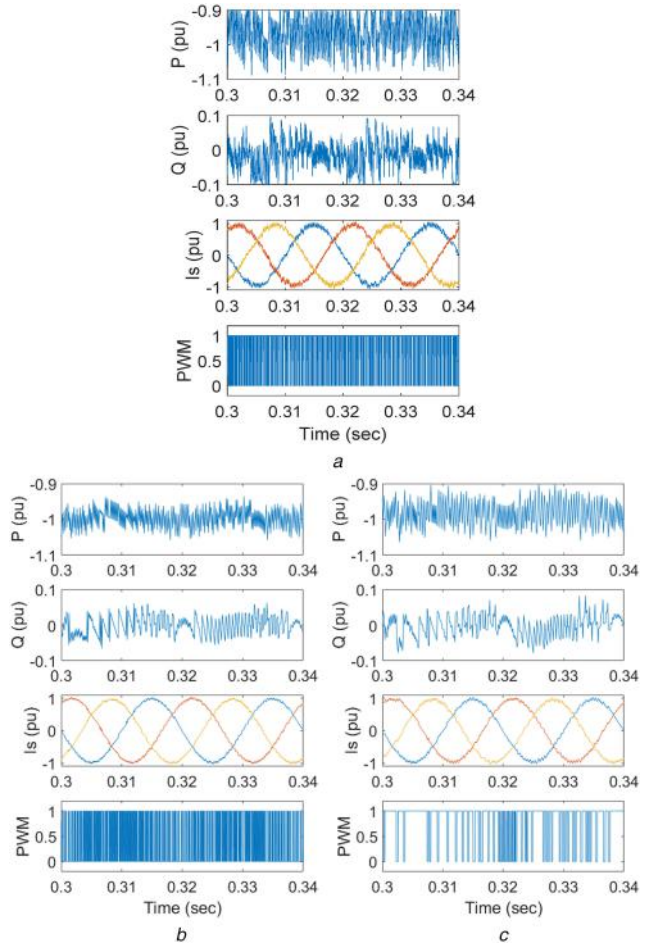

Fig. 10 *Performance of DPC and MOMPC with and without switching frequency reduction scheme*
(a) DPC, ***(b)*** MOMPC using cost function (16), ***(c)*** MOMPC using cost function (34)

pu at 0.3 s and was changed again to −0.5 pu at 0.4 s. Figs. 8*c* and *d* present the detailed dynamic responses under such power variation conditions for both control strategies. It can be seen that for both control methods, the new steady state can be reached in a fast manner without overcurrents in both stator and rotor currents. However, obvious sparks and ripples can be observed in both active and reactive powers for the DPC approach.

To compare the dynamic responses of two methods more precisely, the enlarged waveforms of reactive powers around 0.4 s under the condition of stepped changes are provided as shown in Fig. 9. It is seen that the proposed MOMPC reaches the new reference about 0.5 ms earlier than DPC, showing even quicker dynamic response.

5.7 Switching frequency reduction

It is noted that the switching frequency reduction algorithm of MOMPC has been implemented in MPPT and flexible power regulation operations during the above tests. To demonstrate the effectiveness of the switching frequency reduction scheme, the system performances of DPC and the proposed MOMPC using the cost functions of (16) and (34) are shown in Figs. 10*a–c*, respectively. DPC presents most ripples in active power and reactive power and worst stator current quality with most PWM switchings. As to MOMPC, after adding a non-linear constraint in the cost function to evaluate the switching instants on each leg of the converter, the switching frequency has been reduced significantly, but no major deterioration in powers and currents is observed. This is very useful for high-power DFIG-based wind energy systems as the switching frequency should be restricted to the level of a few hundred hertz to reduce the switching losses to improve the system efficiency.

5.8 Algorithm complexity

To evaluate the complexity of the control strategies, the algorithm computing time in the digital signal processor, T_c, is compared. The C code program is generated in the TI Code Composer Studio (CCS) from the Simulink model in integrated development environment automatically. The program is then downloaded from the CCS into the TMS320F28335 Experimenter Kit for real-time execution. T_c is then calculated using the 'clock' function in the CCS, which is implemented by setting two break points at the beginning and the end of the interrupt service routine where the overall control algorithm is executed. The testing results of algorithm complexity are shown in Table 2. To conduct a comprehensive comparison, the quantitative results of DPC and MOMPC are also summarised in Table 2 including the sampling frequency f_s, average switching frequency f_{sw}, active power ripple P_{rip}, reactive power ripple Q_{rip}, and the THDs of stator and rotor currents. The average switching frequency is calculated by counting the total commutation instants of a phase leg during a fixed period, e.g. 0.05 s. The power ripples are calculated by using the standard deviation. From Table 2, it can be seen that both the stator and rotor current THDs of MOMPC are lower than those of DPC. In addition, smaller active and reactive powers ripples are obtained by using MOMPC, showing better steady-state performance. The most interesting point is that the average switching frequency of MOMPC using the cost function of (34) (i.e. with switching frequency reduction scheme) has been reduced significantly to only about 780 Hz, much lower than 1.96 kHz of MOMPC using (16) as the cost function and 3.75 kHz of DPC. Overall, this demonstrates that the proposed MOMPC method can achieve better performance at much lower switching frequency compared to the conventional DPC approach. This is a very attractive advantage. As the power level of the wind turbines is expected to increase rapidly for large-scale grid integrations, lower switching frequency is more appropriate to reduce the switching losses to improve the system efficiency. For the algorithm complexity, it is seen that all the algorithms can be executed completely within the control period of 100 µs (corresponding to 10 kHz sampling frequency). So the voltage vectors can be determined and updated properly. Specifically, the MOMPC takes about 37 µs computing time, slightly longer than 30 µs of DPC. In other words, MOMPC only consumes <40% of the allowable computing time of 100 µs in every control period. It is worth mentioning that the actual computing time could be different, depending on the computing power of the hardware and the programming style of the researchers. T_c used here is just an indicator to evaluate the complexity of control methods approximately.

6 Conclusion and future work

In this paper, a MOMPC technique for DFIG-based wind energy systems with improved transient and steady-state performance has been proposed. The future behaviours of the DFIGs are predicted

Table 2 Quantitative comparison of different control strategies at grid-connected operation

Strategy	f_s, kHz	f_{sw}, kHz	P_{rip}, pu	Q_{rip}, pu	THD of I_s, %	THD of I_r, %	T_c, μs
DPC	10	3.75	0.0395	0.0325	7.16	9.47	29.8
MOMPC + (16)	10	1.96	0.0215	0.0244	5.25	6.45	36.5
MOMPC + (34)	10	0.78	0.0295	0.0292	5.65	6.90	37.0

based on the system discrete-time model and the possible power converter switching states. The most appropriate voltage vector is then selected according to a cost function to minimise the errors between the reference and the measured values. In the MOMPC, a very flexible and sophisticated cost function is designed so that multiple control objectives, such as the grid synchronisation, active and reactive power regulation, and maximum power generation under various wind speed, are achieved flexibly by changing the power references. In addition, a non-linear constraint is added to the cost function to reduce the switching frequency. A comparison between the proposed MOMPC and the conventional switching table based DPC demonstrates that the proposed method shows faster and smoother grid synchronisation. At grid-connected operation, the power ripples can be reduced, and the stator current THD is reduced from 7.16 to 5.65% at only about 0.78 kHz switching frequency. These merits highlight the potential use in high-power DFIG applications.

The proposed method belongs to component-level control of DFIGs. With more and more wind generators connected to the main grid, the high penetration of such intermittent renewable generation poses new challenges to grid stability. In such a power network, the active power balance must be kept to stabilise the system frequency, and the reactive power should be controlled to maintain the voltage magnitude. As a subsequent work of this research, we will develop system-level control methods for wind generators, and we will test the proposed methods in different standard distribution systems.

7 References

[1] Global Wind Energy Council: 'Global wind energy outlook 2016', November 2016

[2] Song, Z., Xia, C., Shi, T.: 'Assessing transient response of DFIG based wind turbines during voltage dips regarding main flux saturation and rotor deep-bar effect', *Appl. Energy*, 2010, **87**, (10), pp. 3283–3293

[3] Biswas, P.P., Suganthan, P.N., Amaratunga, G.A.J.: 'Optimal power flow solutions incorporating stochastic wind and solar power', *Energy Convers. Manage.*, 2017, **148**, pp. 1194–1207

[4] Jafarian, M., Ranjbar, A.M.: 'Interaction of the dynamics of doubly fed wind generators with power system electromechanical oscillations', *IET Renew. Power Gener.*, 2013, **7**, (2), pp. 89–97

[5] Edrah, M., Lo, K.L., Anaya-Lara, O.: 'Reactive power control of DFIG wind turbines for power oscillation damping under a wide range of operating conditions', *IET. Gener. Transm. Distrib.*, 2016, **10**, (15), pp. 3777–3785

[6] Wu, Z., Li, F., Zhang, W., *et al.*: 'Research on robust adaptive cooperative stabilisation control for doubly-fed induction generator unit', *IET Gener. Transm. Distrib.*, 2017, **12**, (4), pp. 997–1003

[7] Chen, Z., Guerrero, J., Blaabjerg, F.: 'A review of the state of the art of power electronics for wind turbines', *IEEE Trans. Power Electron.*, 2009, **24**, (8), pp. 1859–1875

[8] Ademi, S., Jovanovic, M.: 'A novel sensorless speed controller design for doubly-fed reluctance wind turbine generators', *Energy Convers. Manage.*, 2016, **120**, pp. 229–237

[9] De Doncker, R.W., Muller, S., Deicke, M.: 'Doubly fed induction generator systems for wind turbines', *IEEE Mag. Ind. Appl.*, 2002, **8**, (3), pp. 26–33

[10] Aydin, E., Polat, A., Ergene, L.T.: 'Vector control of DFG in wind power applications and analysis for voltage drop condition'. Proc. of National Conf. on Electrical, Electronics and Biomedical Engineering (ELECO), 2016, pp. 81–85

[11] Abad, G., Rodriguez, M.A., Poza, J.: 'Two-level VSC based predictive direct torque control of the doubly fed induction machine with reduced torque and flux ripples at low constant switching frequency', *IEEE Trans. Power. Electron.*, 2008, **23**, (3), pp. 1050–1061

[12] Boulouiha, H.M., Allalia, A., Laouer, M., *et al.*: 'Direct torque control of multilevel SVPWM inverter in variable speed SCIG-based wind energy conversion system', *Renew. Energy*, 2015, **80**, pp. 140–152

[13] Pimple, B.B., Vekhande, V.Y., Fernandes, B.G.: 'A new direct torque control of doubly fed induction generator for wind power generation'. Proc. India Int. Conf. on Power Electronics, 2011, pp. 1–5

[14] Manel, J.-B.G., Arbi, J., Ilhem, S.-B.: 'A novel approach of direct active and reactive power control allowing the connection of the DFIG to the grid'. Proc. IEEE Power Electronics and Applications Conf., 2009, pp. 1–10

[15] Datta, R., Ranganathan, V.: 'Direct power control of grid-connected wound rotor induction macine without rotor position sensors', *IEEE Trans. Power Electron.*, 2001, **16**, (3), pp. 390–399

[16] Singh, B., Naidu, N.K.S.: 'Direct power control of single VSC-based DFIG without rotor position sensor', *IEEE Trans. Ind. Appl.*, 2014, **50**, (6), pp. 4152–4163

[17] Hu, J., Zhu, J., Zhang, Y., *et al.*: 'Predictive direct virtual torque and power control of doubly fed induction generators for fast and smooth grid synchronization and flexible power regulation', *IEEE Trans. Power Electron.*, 2013, **28**, (7), pp. 3182–3194

[18] Tremblay, E., Atayde, S., Chandra, A.: 'Comparative study of control strategies for the doubly fed induction generator in wind energy conversion systems: a DSP-based implementation approach', *IEEE Trans. Sustain. Energy*, 2011, **2**, (3), pp. 288–299

[19] Abad, G., Rodriguez, M.A., Poza, J.: 'Two-level VSC-based predictive direct power control of the doubly fed induction machine with reduced power ripple at low constant switching frequency', *IEEE Trans. Energy Convers.*, 2008, **23**, (2), pp. 570–580

[20] Zarei, M.E., Nicolas, C.V., Arribas, J.R.: 'Improved predictive direct power control of doubly fed induction generator during unbalanced grid voltage based on four vectors', *IEEE J. Emerging Sel. Top. Power Electron.*, 2017, **5**, (2), pp. 695–707

[21] Kujundzic, G., Iles, S., Matusko, J., *et al.*: 'Optimal charging of valve-regulated lead-acid batteries based on model predictive control', *Appl. Energy*, 2017, **187**, pp. 189–202

[22] Zhang, S., Xiong, R., Zun, F.: 'Model predictive control for power management in a plug-in hybrid electric vehicle with a hybrid energy storage system', *Appl. Energy*, 2017, **185**, pp. 1654–1662

[23] Filho, A.J.S., Filho, E.R.: 'Model-based predictive control applied to the doubly-fed induction generator direct power control', *IEEE Trans. Sustain. Energy*, 2012, **3**, (3), pp. 398–406

[24] Errouissi, R., Al-Durra, A., Muyeen, S.M., *et al.*: 'Offset-free direct power control of DFIG under continuous-time model predictive control', *IEEE Trans. Power Electron.*, 2017, **32**, (3), pp. 2265–2277

[25] Liu, Q., Hameyer, K.: 'Torque ripple minimization for direct torque control of PMSM with modified FCSMPC', *IEEE Trans. Ind. Appl.*, 2016, **52**, (6), pp. 4855–4864

[26] Sayari, N.A., Chilipi, R., Barara, M.: 'An adaptive control algorithm for grid-interfacing inverters in renewable energy based distributed generation systems', *Energy Convers. Manage..*, 2016, **111**, pp. 443–452

[27] Ostolaza, J.X., Etxeberria, A., Zubia, I.: 'Wind farm node connected DFIG/ back-to-back converter coupling transient model for grid integration studies', *Energy Convers. Manage..*, 2015, **106**, pp. 428–439

[28] Muttaqi, K.M., Hagh, M.T.: 'A synchronization control technique for soft connection of doubly-fed induction generator based wind turbines to the power grid'. IEEE Ind. Appl. Society Annual Meeting, 2017, pp. 1–7

[29] Saglam, U.: 'Assessment of the productive efficiency of large wind farms in the United States: an application of two-stage data envelopment analysis', *Energy Convers. Manage.*, 2017, **153**, pp. 188–214

[30] Wandhare, R.G., Agarwal, V.: 'Novel integration of a pv-wind energy system with enhanced efficiency', *IEEE Trans. Power Electron.*, 2015, **30**, (7), pp. 3638–3649

[31] Fathabadi, H.: 'Novel photovoltaic based battery charger including novel high efficiency step-up dc/dc converter and novel high accurate fast maximum power point tracking controller', *Energy Convers. Manage.*, 2016, **110**, pp. 200–211